

See discussions, stats, and author profiles for this publication at:
<https://www.researchgate.net/publication/223693994>

Fatigue damage modeling in solder interconnects using a cohesive zone approach

Article in *International Journal of Solids and Structures* · February 2005

DOI: 10.1016/j.ijsolstr.2004.07.026

CITATIONS

70

READS

31

3 authors, including:



Adnan Jawdat Judeh

Environment Quality Authority - Palestine

20 PUBLICATIONS 262 CITATIONS

[SEE PROFILE](#)



Marc G. D. Geers

Technische Universiteit Eindhoven

518 PUBLICATIONS 8,014 CITATIONS

[SEE PROFILE](#)

Some of the authors of this publication are also working on these related projects:



A multi-scale study on the effects of humidity on the mechanics of paper [View project](#)



Fundamentals of a fluctuation enriched computational homogenization [View project](#)

All content following this page was uploaded by **Adnan Jawdat Judeh** on 26 September 2016.

The user has requested enhancement of the downloaded file. All in-text references **underlined in blue** are added to the original document and are linked to publications on ResearchGate, letting you access and read them immediately.



Fatigue damage modeling in solder interconnects using a cohesive zone approach

A. Abdul-Baqi, P.J.G. Schreurs *, M.G.D. Geers

*Department of Mechanical Engineering, Section of Materials Technology, Eindhoven University of Technology,
P.O. Box 513, 5600 MB, Eindhoven, The Netherlands*

Received 19 May 2003; received in revised form 13 July 2004
Available online 12 October 2004

Abstract

The objective of this work is to model the fatigue damage process in a solder bump subjected to cyclic loading conditions. Fatigue damage is simulated using the cohesive zone methodology. Damage is assumed to occur at interfaces modeled through cohesive zones in the material, while the bulk material is assumed to be linear elastic. The state of damage at a cohesive zone is incorporated into the cohesive zone constitutive law by a elasticity-based damage variable. The gradual degradation of the solder material and the corresponding damage accumulation throughout the cycling process is accounted for by a damage evolution law which captures the main damage characteristics. The model prediction of the solder bump life-time is shown to be in good agreement with one of the commonly used empirical life-time prediction laws.

© 2004 Elsevier Ltd. All rights reserved.

Keywords: Cohesive zone; Fatigue damage; Solder joint; Life-time

1. Introduction

In the electronics industry, reliability of an IC package is usually determined through the integrity of its solder joint interconnects. The latter have the function of providing both electrical and mechanical connections between the silicon chip and the printed circuit board. Repeated switching of the electronic device leads to temperature fluctuations which, combined with the mismatch of the coefficients of thermal expansion (CTE), will result in stresses causing fatigue of the solder joints. Progressive damage will eventually

* Corresponding author. Tel.: +31 40 247 2778; fax: +31 40 244 7355.
E-mail address: p.j.g.schreurs@tue.nl (P.J.G. Schreurs).

result in a device failure. This problem is becoming increasingly important as the flux of the dissipated energy in the solder joints is increasing due to miniaturization.

Numerical prediction of fatigue life-time of solder joints generally consists of four main steps. Firstly, a constitutive model which describes the solder material behavior is chosen. Secondly, one loading cycle is simulated using the finite element method (FEM), where the stresses and the strains in the material are calculated. Thirdly, from the calculated stresses and/or strains, the number of cycles to failure N_f is calculated based on a selected fatigue life prediction model. A review of such models can be found in Lee et al. (2000). Finally, the model prediction is verified using experimental thermal cycling data. This approach is the most popular among other existing approaches for fatigue analysis of solder joints. This is mainly due to its simplicity and relatively short computing time. However, there is a major drawback associated with this approach. The stresses and strains are calculated from a single loading cycle and the material properties of the solder are assumed to remain constant during the successive cycles. This assumption results in underestimated values of the fatigue life because in reality, repeated cycling results in a gradual degradation of the solder material (Basaran et al., 2001). This has been emphasized experimentally through the observation that creep hysteresis loops of solder materials collapse over the thermal cycles (Zhang et al., 2000). Moreover, solder joint fatigue models were developed based on experimental thermal cycling tests on macroscopic specimens. The applicability of such models to a solder joint has not yet been justified. More realistic models should account for the microstructural evolution of the solder material during the process of cycling. During thermal and/or mechanical cyclic loading, the solder material undergoes phase separation and severe coarsening at an early stage of the cycling process (Matin et al., 2003; Ubachs et al., 2003). The coarsening of the solder microstructure eventually leads to stress concentrations in the material which, in addition to the localization of the interfaces with the coarsened phases, will contribute severely to the fatigue damage. The incorporation of all such phenomena explicitly in a fatigue model is rather complicated. Instead, this can be achieved partially by adopting a continuum damage approach, for example, where the microstructural changes and the corresponding material degradation are accounted for in the constitutive material model itself by a damage variable. However, besides the requirement of extensive computations, the choice of a damage variable and a damage evolution law is quite arbitrary and experimental verifications are usually not available.

The cohesive zone method is a numerical tool for the mechanics of interfaces, that was initially developed to model crack initiation and growth. This method treats fracture as a gradual process in which separation between incipient material surfaces is resisted by cohesive tractions (Nguyen et al., 2001). It is a typical interfacial damage model, which can be situated between continuum damage mechanics and fracture mechanics. In comparison with fracture mechanics, the cohesive zone method has the advantages of smoothing the stress singularities at the crack tip and the easy adaptability to material and geometrical nonlinearities (Chaboche et al., 2001). Compared to continuum damage mechanics, the cohesive zone method can be used to model cracking at interfaces between dissimilar materials. The fracture characteristics of the material such as fracture energy (the area under the traction curve) and fracture strength (the peak cohesive traction) are included in a typical cohesive zone constitutive relation. Consequently, crack initiation and crack growth emerge as natural outcomes of the boundary value problem solution without any separate criteria. In the past decade, the cohesive zone method was mainly applied to model cracking under monotonic loading conditions (Abdul-Baqi, 2002; Chaboche et al., 2001; Tijssens, 2000; Xu and Needleman, 1993). The applicability of this method to fatigue damage under cyclic loading has only quite recently started to receive some attention (de Andres et al., 1999; Nguyen et al., 2001; Roe and Siegmund, 2003; Yang et al., 2000). Damage, as a dissipative mechanism, can be accounted for explicitly by incorporating a damage variable into the cohesive zone constitutive law (Roe and Siegmund, 2003). According to this approach the peak cohesive traction and cohesive energy are assumed to diminish with the damage parameter. The damage is determined using an evolution law in which the damage rate is a function of the cohesive parameters. An other way to account for damage is to include an unloading–reloading hysteresis into

the cohesive zone law (de Andres et al., 1999; Nguyen et al., 2001; Yang et al., 2000), that simulates the accumulation of damage within the cohesive zone which eventually leads to complete failure.

The objective of the present paper is to model the fatigue damage process in a solder bump subjected to cyclic loading. For this purpose we perform a numerical simulation of the load cycling process using the finite element method. Damage in the bump is modeled using the cohesive zone methodology. Degradation of the solder material throughout the cycling process is accounted for by the incorporation of a damage variable into the cohesive zone constitutive law. The damage variable is supplemented by an evolution law to account for the accumulation of damage. The evolution law is typically phenomenological and is formulated in a way which takes into account the main damage characteristics. The cohesive zone description proposed is applicable for quasi-brittle interfaces, i.e., where a degradation mechanism without noticeable permanent deformations is dominant. The presented model presents itself in a somewhat simpler format than the Roe and Sigmund (Roe and Siegmund, 2003) approach, even though the damage evolution law is more sophisticated. Damage evolution can be described for both normal and tangential directions separately. The evolution law contains more parameters, which can be used to describe the damage evolution more accurately, especially at the final stage of the life-time. Damage distribution in the solder bump is presented at different loading cycles and at complete failure. The decrease of the reaction force with the number of cycles is illustrated as a measure of the overall loss of stiffness. Finally, the life-time prediction capability of the model is compared with the prediction of one of the commonly used classical models, a Coffin–Manson law. So far, the analysis is limited to a two-dimensional configuration, where the third dimension is constrained through a plane strain assumption.

2. Problem formulation

Solder materials undergo continuous microstructural coarsening during loading. Fig. 1 illustrates such coarsened microstructure for a eutectic tin–lead (Sn–Pb) solder after only 48 h of thermal ageing. For numerical convenience, the present simulations are performed on a rather simplified microstructure as illustrated in Fig. 2. A single solder bump is modeled in plane-strain which is an approximation of the actual three-dimensional problem. The solder material which is assumed to be a eutectic tin–lead solder is

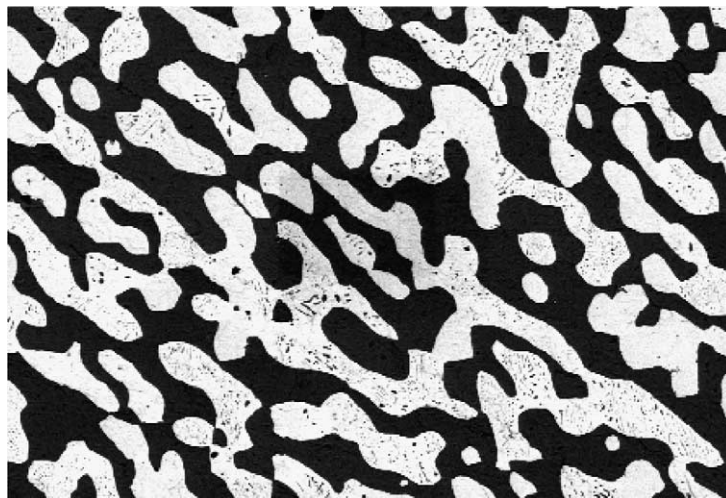


Fig. 1. Tin–lead solder with the white region being the lead-rich phase (Matin et al., 2003).

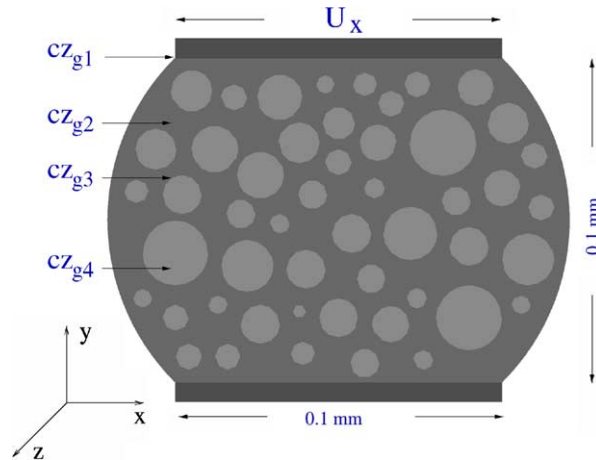


Fig. 2. Modeled geometry.

idealized as a well-defined two-phase system. The inclusions are assumed to be the lead-rich phase, while the surrounding bulk is the tin-rich phase. Fatigue damage in the bump is modeled using a cohesive zone approach as explained in Section 2.1. Cohesive zones are embedded at physical boundaries in the solder bump (interfaces with the upper and lower boundaries and interfaces with the second phase inclusions) as well as at the grain boundaries of the same phase. Experimentally, it has been observed that fatigue damage indeed localizes at these physical interfaces, which motivates the use of the cohesive zone approach adopted here. Cyclic loading is applied in terms of sinusoidal shear displacement which is prescribed incrementally along the upper boundary while keeping the lower boundary fixed.

The bump material is assumed to be linear elastic with a Young’s modulus $E = 50 \text{ GPa}$ and a Poisson’s ratio $\nu = 0.36$ for the bulk (tin phase) and $E = 16 \text{ GPa}$ and $\nu = 0.44$ for the inclusions (lead phase). The upper and lower layers are assigned the same values as those of tin. Evidently, the full characterization of solder joint fatigue would necessitate the incorporation of cyclic thermal loading and temperature related material modeling (creep) and consequently the quantification of temperature dependent material parameters. Temperature and rate dependence are not yet incorporated in this framework. Even though the bulk phases indeed show a typically viscoplastic response, failure is experimentally found to localize at physical interfaces (interphase boundaries, colony boundaries, etc.), where the proposed model serves as a good first approximate.

The sinusoidal shear displacement has an amplitude of $1.0 \mu\text{m}$ which results in a maximum applied shear strain $\epsilon_{\text{max}} = 1.0\%$. The analysis is carried out numerically using the finite element method. It uses a total Lagrangian formulation in which equilibrium is expressed in terms of the principle of the virtual work as

$$\int_v \sigma_{ij} \delta \epsilon_{ij} dv + \int_{S_i} T_\alpha \delta \Delta_\alpha dS = \int_{\partial v} t_i \delta u_i ds \tag{1}$$

Here, v is the total region analyzed and ∂v is its external boundary. With $x_i = (x, y, z)$ the coordinates, u_i and t_i are the components of displacement and traction vector, respectively; σ_{ij} are the components of Cauchy stress while ϵ_{ij} are the linear strain components. The latter are expressed in terms of the displacement fields in the standard manner,

$$\epsilon_{ij} = \frac{1}{2} \left(\frac{\partial u_i}{\partial x_j} + \frac{\partial u_j}{\partial x_i} \right) \tag{2}$$

The second term in the left-hand side of Eq. (1) is the contribution of the cohesive zones. The traction transmitted across a cohesive zone has components T_α , while the opening displacement is Δ_α , both measured in a local frame of reference at the cohesive zone. The cohesive zone nodal force vector and stiffness matrix are derived in Section 2.2.

The previous equations, completed with the constitutive law for the cohesive zones to be discussed further on, form a nonlinear problem that is solved incrementally using the rate form of the virtual work in Eq. (1). The numerical procedure used to solve the present boundary value problem follows the one used by Wu and van der Giessen (1996).

2.1. Cohesive tractions and damage evolution

A cohesive zone is a four-noded element (Fig. 3) with zero initial thickness ($\Delta = 0$). Its constitutive behavior is specified through a relation between the relative opening displacement Δ_α and a corresponding traction T_α at the same location, with α being either the local normal (n) or tangential (t) direction in the cohesive zone plane (Abdul-Baqi, 2002). For the case of monotonic loading, the cohesive traction is characterized mainly by a peak value which represents the cohesive strength and a cohesive energy. An example of such tractions are those given by Xu and Needleman (1993):

$$T_n = \sigma_{\max} \exp(1) \frac{\Delta_n}{\delta_n} \exp\left(-\frac{\Delta_n}{\delta_n}\right) \tag{3}$$

$$T_t = \tau_{\max} \sqrt{2 \exp(1)} \frac{\Delta_t}{\delta_t} \exp\left(-\frac{\Delta_t^2}{\delta_t^2}\right) \tag{4}$$

where δ_n and δ_t are characteristic lengths, σ_{\max} and τ_{\max} are the peak tractions in the normal and tangential directions, respectively. Energy dissipation is accounted for by the softening branch in the curve as illustrated in Fig. 4. Under monotonic loading, the cohesive traction reaches a peak value when a critical opening displacement is attained then starts to diminish with the gradual increase of the opening displacement. This will result in the creation of two traction-free surfaces which marks the initiation of a crack or the extension of an existing one.

Under cyclic loading, the situation is rather different. If the applied traction is less than the cohesive strength, the cohesive zone will have an infinite life. Fatigue experiments, however, indicate that under cyclic loading materials fail at stress levels below their static fracture strength (Ellyin, 1997) which is essentially

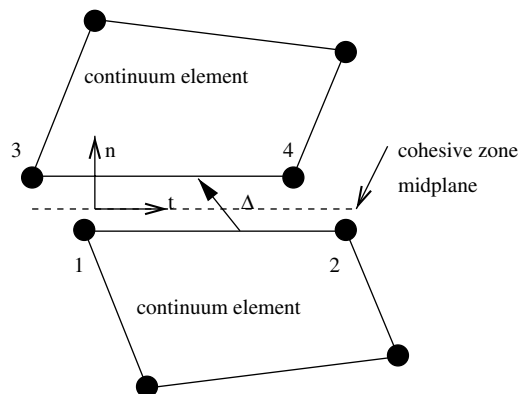


Fig. 3. Cohesive zone illustration. (t, n) is a local frame of reference defined such that the t -axis lies in the cohesive zone midplane.

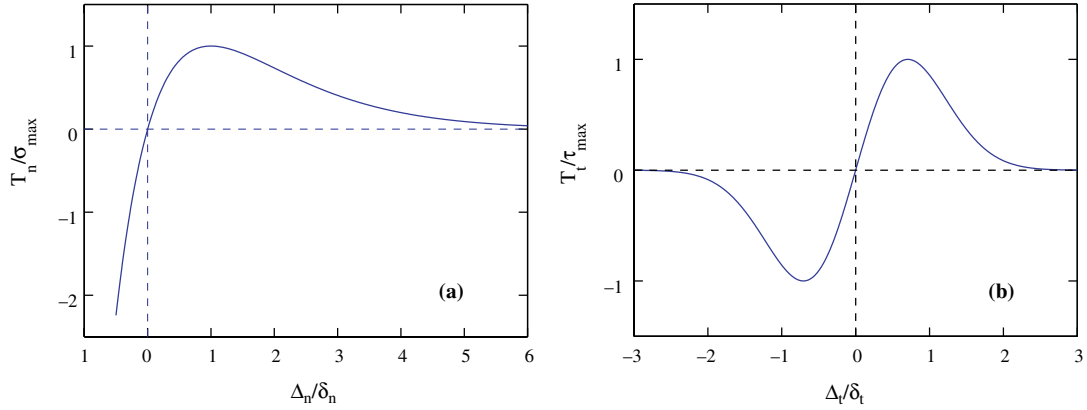


Fig. 4. Cohesive zone monotonic normal (a) and shear (b) tractions.

due to creep damage. Following the formulation of [Chaboche et al. \(2001\)](#), in the present study we adopt a constitutive law in which the traction is a linear function of the separation, whereas the energy dissipation is accounted for by the incorporation of a nonlinear damage variable into the constitutive law:

$$T_\alpha = k_\alpha(1 - D_\alpha)\Delta_\alpha \tag{5}$$

where k_α is the initial stiffness of the cohesive zone and D_α is the damage variable. D_α varies between zero (0) for damage-free cohesive zones and one (1) for completely damaged zones. In this formulation, energy dissipation associated with the gradual degradation of the solder material is accounted for by the damage variable D_α only. An additional softening branch emerging from a nonlinear traction law would add an additional energy dissipation mechanism.

The damage variable is supplemented with an evolution law to account for the accumulation of damage throughout the cycling process. Motivated by the formulation of [Roe and Siegmund \(2003\)](#), the following evolution law is here adopted:

$$\dot{D}_\alpha = c_\alpha |\dot{\Delta}_\alpha| (1 - D_\alpha + r)^m \left(\frac{|T_\alpha|}{1 - D_\alpha} - \sigma_f \right) \tag{6}$$

where c_α is a constant which controls the damage accumulation, $\dot{\Delta}_\alpha$ is the rate of the relative opening of the cohesive zone, r and m are constants which control the decay of the reaction force at the final stage of damage and σ_f is the cohesive zone endurance limit ([Roe and Siegmund, 2003](#)). Note that static strength of the cohesive zone, i.e., the maximum load after which abrupt softening would occur, is never reached in this model. In practice, this assumption is based on the fact that the bulk material of interest will yield and deform plastically before this maximum load is reached. Note that monotonous damage relies on different dissipation mechanisms, which can be added to the model in a similar manner as [Roe and Sigmund](#) did. Since these mechanisms are not considered here, monotonous damage has been ignored. In the next section, the main features of the damage evolution law (Eq. (6)) together with the traction separation law (Eq. (5)) are examined against the main cyclic damage characteristics.

2.2. Cohesive zone virtual work

The contribution of the cohesive zones to the virtual work principle in Eq. (1) is determined by calculating the cohesive zone stiffness matrix and internal nodal force vector. In the local frame of reference (t, n) illustrated in [Fig. 3](#), the cohesive element nodal displacement vector is given by

$$\mathbf{u}_l^T = \{u_t^1, u_n^1, u_t^2, u_n^2, u_t^3, u_n^3, u_t^4, u_n^4\} \tag{7}$$

where subscript l denote quantities in the local frame of reference. The local relative displacement vector Δ is given as

$$\Delta = \begin{Bmatrix} \Delta_t \\ \Delta_n \end{Bmatrix} = \mathbf{A}\mathbf{u}_l \tag{8}$$

where \mathbf{A} is a matrix of the shape functions given as

$$\mathbf{A} = \begin{bmatrix} -h_1 & 0 & -h_2 & 0 & h_1 & 0 & h_2 & 0 \\ 0 & -h_1 & 0 & -h_2 & 0 & h_1 & 0 & h_2 \end{bmatrix} \tag{9}$$

and

$$h_1 = \frac{1}{2}(1 - \eta), \quad h_2 = \frac{1}{2}(1 + \eta) \tag{10}$$

The parameter η is defined at the cohesive zone mid plane and varies between -1 at nodes (1,3) and 1 at nodes (2,4).

The element internal nodal force vector and stiffness matrix are now written as

$$\mathbf{f}_l = \int_S \mathbf{A}^T \mathbf{T} dS = \frac{l}{2} \int_{-1}^{+1} \mathbf{A}^T \mathbf{T} d\eta \tag{11}$$

$$\mathbf{K}_l = \int_S \mathbf{A}^T \mathbf{D} \mathbf{A} dS = \frac{l}{2} \int_{-1}^{+1} \mathbf{A}^T \mathbf{D} \mathbf{A} d\eta \tag{12}$$

where \mathbf{T} is the traction vector corresponding to the displacement Δ and calculated via Eq. (5), S is the cohesive zone area and l is the cohesive zone length. This formulation is for plane-strain conditions and the cohesive zones are assumed to have a unit thickness. \mathbf{D} is the cohesive zone constitutive tangent operator that relates the incremental variations of the tractions, $d\mathbf{T}$, to the incremental variations of the displacements, $d\Delta$, within the cohesive zone as

$$d\mathbf{T} = \mathbf{D}d\Delta, \tag{13}$$

where

$$\mathbf{D} = \begin{bmatrix} \frac{\partial T_t}{\partial \Delta_t} & \frac{\partial T_t}{\partial \Delta_n} \\ \frac{\partial T_n}{\partial \Delta_t} & \frac{\partial T_n}{\partial \Delta_n} \end{bmatrix}. \tag{14}$$

The integrals in Eqs. (11) and (12) are evaluated using Gaussian integration. Once the element internal nodal force vector \mathbf{f}_l and stiffness matrix \mathbf{K}_l are constructed in the local frame of reference (t, n), they are transformed to the global frame of reference (x, y, z) as

$$\mathbf{f} = \mathbf{R}^T \mathbf{f}_l \tag{15}$$

$$\mathbf{K} = \mathbf{R}^T \mathbf{K}_l \mathbf{R} \tag{16}$$

$$\mathbf{R} = \begin{bmatrix} \mathbf{R}' & \mathbf{0} & \mathbf{0} & \mathbf{0} \\ \mathbf{0} & \mathbf{R}' & \mathbf{0} & \mathbf{0} \\ \mathbf{0} & \mathbf{0} & \mathbf{R}' & \mathbf{0} \\ \mathbf{0} & \mathbf{0} & \mathbf{0} & \mathbf{R}' \end{bmatrix} \quad (17)$$

where \mathbf{R}' is the rotation matrix which relates the local frame to the global frame and is given in terms of the angle θ between the t - and x -axes

$$\mathbf{R}' = \begin{bmatrix} \cos \theta & \sin \theta \\ -\sin \theta & \cos \theta \end{bmatrix} \quad (18)$$

3. Results and discussion

3.1. Uniaxial cyclic tension–compression

In this section, the fatigue damage constitutive model is demonstrated in a one-dimensional case as illustrated in Fig. 5. The bar has a length $L = 2 \times 10^{-2}$ mm and a radius $R = 10^{-2}$ mm. It is assumed to be linear elastic with $E = 30$ GPa and $\nu = 0.25$. Loading is applied in terms of a sinusoidal axial displacement U with an amplitude $U_0 = 2 \times 10^{-4}$ mm. A single cohesive zone with an initial stiffness $k = 10^6$ GPa/mm is placed in the middle of the bar to account for fatigue damage. The value taken for the initial stiffness will be commented on later in this section. For the damage evolution law (Eq. (6)) we have used $c = 100$ mm/N, $\sigma_f = 150$ MPa, $r = 10^{-3}$ and $m = 3$. In this section, subscripts are irrelevant and hence omitted.

The initial stiffness of the cohesive zones has to be sufficiently high in order to diminish their artificial enhancement of the overall compliance (Tijssens, 2000; Xu and Needleman, 1993). In this one-dimensional model, this enhancement can be analytically assessed from the stress continuity requirement. If we assume

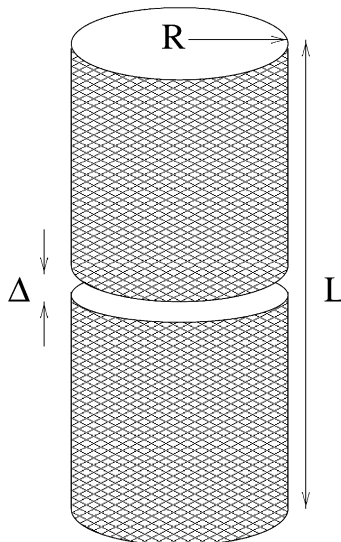


Fig. 5. Uniaxial tension–compression bar.

that the bar contains n equally spaced cohesive zones, each having the same opening Δ , the stress σ in the continuum and the traction T at the cohesive zone are given by:

$$\sigma = \frac{(U - n\Delta)}{L} E \tag{19}$$

$$T = k(1 - D)\Delta \tag{20}$$

After the opening Δ is obtained from the continuity requirement, $\sigma = T$, and substituted in Eq. (19), we get an expression for the stress, $\sigma = (U/L)E^*$, where E^* is an apparent elastic modulus given as

$$E^* = \left(1 - \frac{1}{\frac{kL}{nE}(1 - D) + 1} \right) E \tag{21}$$

To ensure a negligible enhancement of the overall compliance, it is essential that the condition $\frac{nE}{kL} \ll 1$ is satisfied. For the parameters used in this section, $\frac{nE}{kL} = 1.5 \times 10^{-3}$, which is sufficiently small. In a two-dimensional model the condition is estimated by $\frac{E}{kl} \ll 1$, where $l \approx L/n$ is the average cohesive zone length.

The evolution of damage with the number of load cycles is shown in Fig. 6(a). In agreement with experimental observations (Kanchanomai et al., 2002), the presence of a mean strain is seen to cause more damage. Eq. (6) results in a nonlinear damage accumulation as illustrated in Fig. 6(b). In the high–low (H–L) sequence, 200 cycles are applied at a strain of 1% then followed by 200 cycles at 0.5% strain. The order is reversed for the (L–H) sequence. The model prediction is in agreement with experimental observations which indicate that cycling at a high stress level followed by cycling at a lower level (H–L) causes more damage than when the order is reversed (L–H) (Fatemi and Yang, 1998). This is explained by the fact that microcracks are generated during the first loading block and grow during the second block. Starting with the high loading block will cause more microcracks which will eventually grow during the second block causing more damage in the material. Assuming a zero value of the endurance limit σ_f in Eq. (6), both load sequences would result in the same amount of damage. In this case, damage accumulation would be linear as assumed in the classical Miner’s law. It is stated in Lemaitre (1996) that all damage laws of the following general shape show a property of linear accumulation:

$$\dot{D} = f_1(D)f_2(x)\dot{x} \tag{22}$$

where x can either be a stress or a strain. For $\sigma_f = 0$, Eq. (6) can be rewritten in the form of Eq. (22).

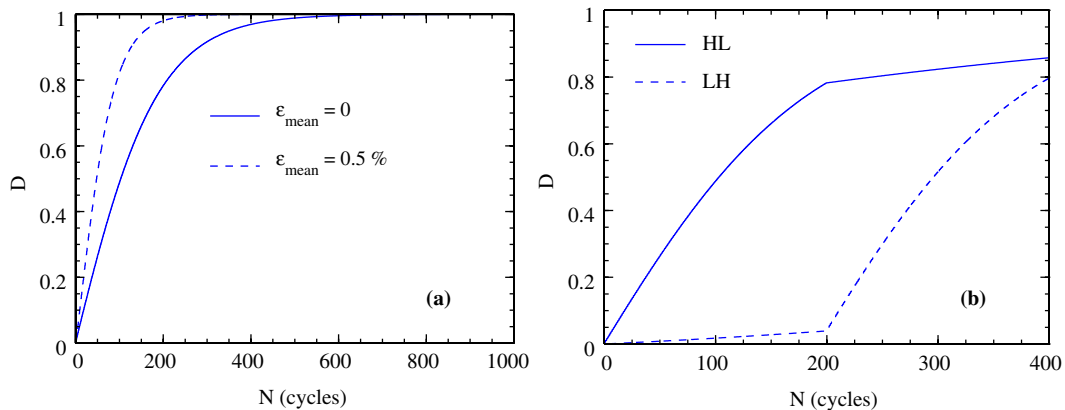


Fig. 6. Damage evolution with loading cycles. (a) Mean strain effect and (b) load sequencing effect.

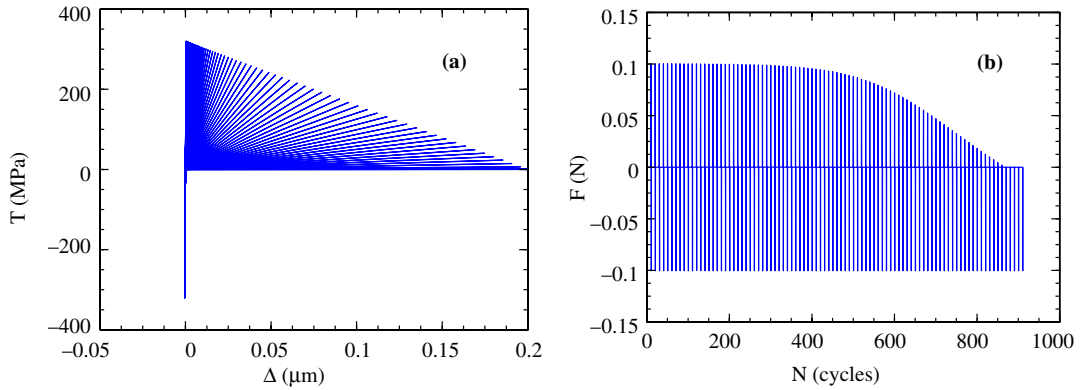


Fig. 7. (a) Cohesive traction versus opening and (b) reaction force versus the number of cycles.

The cohesive traction is shown in Fig. 7(a) as a function of the opening displacement Δ . As damage increases gradually to one, the stiffness and traction diminish to zero. Under compression, the cohesive zone is assumed to maintain its initial stiffness as also seen in Fig. 7(a). This is achieved by using a zero value for the damage variable in Eq. (6) whenever the relative opening displacement Δ is negative. The physical interpretation of this assumption is that the cohesive zone does not soften under compression. Numerically, it minimizes the interpenetration of neighboring continuum elements when they are in a compression state. This assumption is based on the monotonic normal traction shown in Fig. 4(a), in which the stiffness in the negative Δ region is maintained high. The maximum traction in Fig. 7(a) is seen to decrease linearly with the maximum opening displacement. This relation is also reflected in Eq. (19). The decrease of the reaction force is shown in Fig. 7(b). The figure shows a slow decrease at the initial loading stage followed by rapid decrease. This behavior is governed by both the constants m and r in the evolution law. Lower value of the exponent m leads to a brittle-like behavior in which the force will suddenly drop to zero. This is illustrated in Fig. 8(a) for $m = 1$. For $r = 0$, the behavior is illustrated in Fig. 8(b). The rapid decrease stage of the reaction force is followed by a stage of very slow decrease.

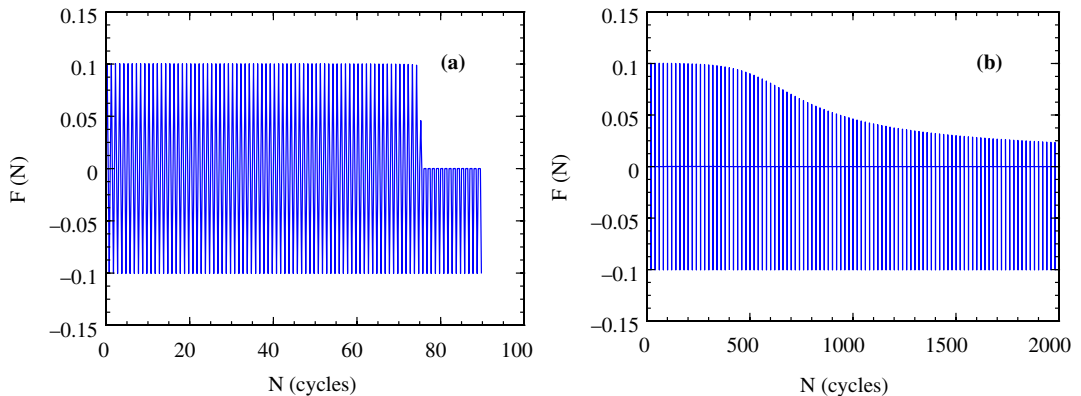


Fig. 8. Reaction force versus the number of cycles for two combinations of the constants r and m in the damage law. (a) $r = 10^{-3}$, $m = 1$ and (b) $r = 0$, $m = 3$.

3.2. Damage in a solder bump

The bump model (Fig. 2) is analyzed using quadrilateral four-node elements. Cohesive zones are placed along physical interfaces, i.e., grain boundaries, phase boundaries and colony boundaries. Consequently, each element represents a physical domain which is characteristic for the underlying microstructure. The finite element discretization is therefore inherently coupled to the microstructure.

Cohesive zones in the solder bump are assigned the same value for the initial stiffness $k_\alpha = 10^6$ GPa/mm. This stiffness is sufficiently high compared to the continuum stiffness such that, in the absence of damage, the cohesive zones artificial enhancement of the overall compliance is negligible. For the current geometry (Fig. 2), this has been verified through the observation that using higher values for the initial stiffness has led to identical reaction forces at the first cycle.

The distinction between the different cohesive zone groups is made by assigning different values for the coefficient c_α in the evolution law. For those at the interfaces with the upper and lower boundaries (i.e. at the Copper pads), $c_{z_{g1}}$ in Fig. 2, $c_\alpha = 0$. This is to prevent the early failure at these locations which is not observed in practice, which would diminish the load transmitted to the bump and hence would stop the propagation of damage into the bump. Inside the bump, cohesive zones at the interface with the second phase inclusions (i.e. the interphase boundary), $c_{z_{g3}}$, are assigned the highest value $c_\alpha = 100$ mm/N. This is based on experimental observations in which fatigue damage is found to occur mainly along these interfaces. Inside the inclusions (i.e. the grain boundaries of the lead-rich phase), $c_{z_{g3}}$, $c_\alpha = 0$. For the group $c_{z_{g2}}$ (i.e. the grain boundaries of the tin-rich phase), $c_\alpha = 25$ mm/N. The remaining parameters are $\sigma_f = 0$, $r = 10^{-3}$ and $m = 3$. For each group the above parameters assume the same value in the tangential ($\alpha = t$) and in the normal ($\alpha = n$) directions.

The detailed simulation of an individual cycle is time consuming, especially for a large number of cycles. In order to reduce the computational time, a method is adopted where only selected cycles are simulated and the contribution of others is extrapolated. Damage is the only history dependent variable in the simulation and hence it is the only extrapolated one. After a detailed simulation of a specific number of cycles, the damage variable $D_\alpha(N)$ is fitted with the cycle number by a third-degree polynomial using the data of the previous 10 cycles. Now the cycle number is increased by an increment ΔN and the damage variable at the current cycle is extrapolated as $D_\alpha(N + \Delta N)$. The increment of cycles is chosen so that the damage increment $D_\alpha(N + \Delta N) - D_\alpha(N)$ is sufficiently small (de Andres et al., 1999).

The distribution of damage at different cycles is shown in Fig. 9. At each cohesive zone an effective damage value is calculated from the normal and tangential damage components at that location as

$$D_{\text{eff}}^i = (D_t^i{}^2 + D_n^i{}^2 - D_t^i D_n^i)^{1/2}. \quad (23)$$

A cohesive zone (i) is marked as damaged when $D_{\text{eff}}^i \geq 0.5$. Fig. 9 shows that damage initiates close to the upper and lower boundaries and at the center of the bump. Later on, damage propagates to the interfaces with the second phase inclusions, then throughout the entire bump leading to complete failure.

As damage progresses in the solder bump, the overall stiffness decreases and the load required to attain the same strain level decreases as shown in Fig. 10. The figure shows a slow softening at the initial stage followed by rapid softening. This qualitative behavior is in agreement with experimental observations on tin–lead solder alloys (Kanchanomai et al., 2002).

An effective measure of the total damage in the solder bump is computed by averaging the effective damage given by Eq. (23) over the entire bump, i.e.,

$$D_{\text{eff}} = \frac{1}{A} \sum_{i=1}^{N_{cz}} D_{\text{eff}}^i A^i \quad (24)$$

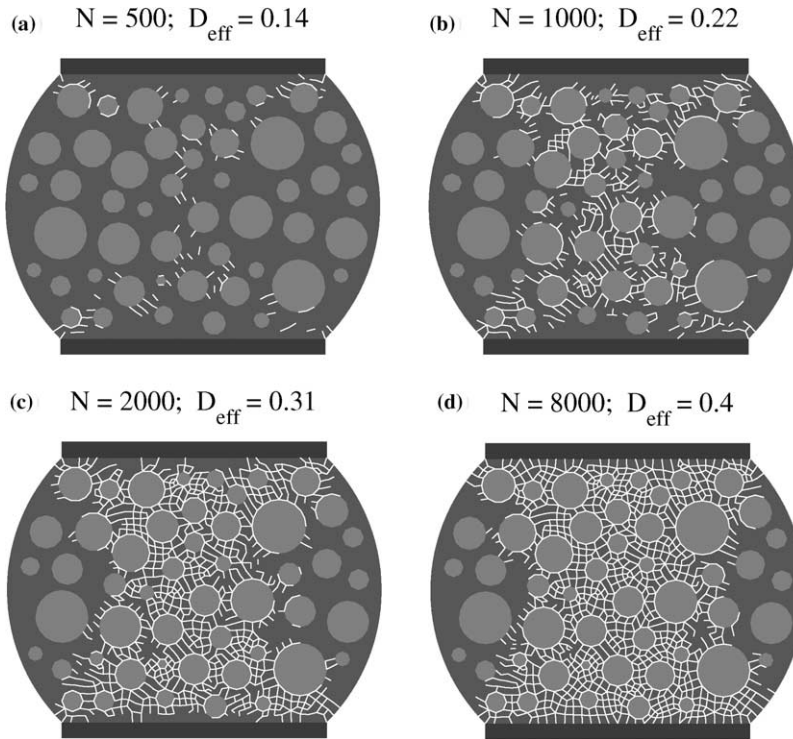


Fig. 9. Damage distribution in the solder bump at different cycles. White lines indicate damaged cohesive zones.

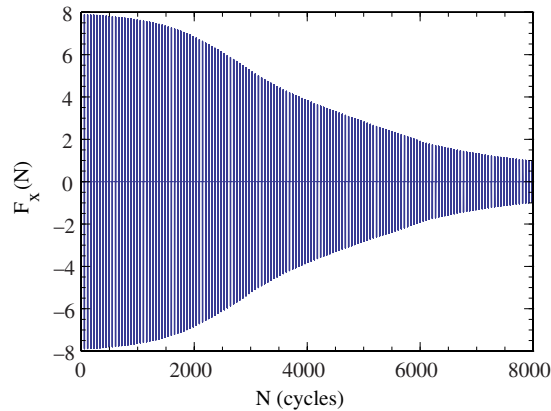


Fig. 10. The reaction force versus the number of cycles.

where A^i is the i th cohesive zone area, A is the total area and N_{cz} is the number of cohesive zones. The evolution of the total effective damage throughout the cycling process is shown in Fig. 11. The figure shows a rapid increase of damage at the initial cycling stage and a much slower increase at the final stage. This can be explained by the fact that initially more cohesive zones are damaged as the load is transmitted through the entire bump. At a later stage all cohesive zones close to the boundaries are damaged as seen in the

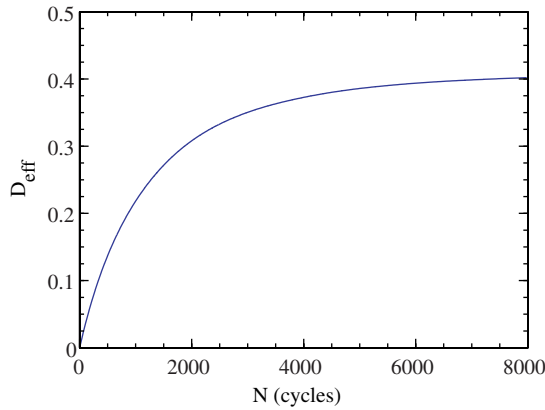


Fig. 11. The total effective damage versus the number of cycles.

Figure after 2000 cycles. The load transmitted through these damaged bands starts to decrease rapidly. As a consequence, the deformation of the cohesive zones in between decreases as well as their contribution to the total damage. The latter is a typical illustration of the localization that develops progressively in fatigue.

To establish the number of cycles to failure and the associated fatigue life-time, an appropriate fatigue failure criterion has to be chosen. As the simulation is performed under strain-controlled conditions, the decrease of the reaction force has been chosen as a failure indicator. Failure of the bump is assumed to occur when the reaction force reaches a critical value. This value is taken as 50% of the maximum force at the first cycle (Kanchanomai et al., 2002; Lee et al., 2000). For an applied strain ϵ_{\max} ranging from 0.2% to 10% the corresponding number of cycles to failure N_f is calculated. The results presented in Fig. 12 follow a typical (S–N) type of behavior and they are well-fitted with a Coffin–Manson model,

$$\epsilon_{\max} = a(2N_f)^b \tag{25}$$

where a is the fatigue ductility coefficient and b is the fatigue ductility exponent. In here, ϵ_{\max} is the maximum overall strain, which is defined as the maximum applied displacement divided by the solder bump’s width. The sensitivity of the parameters a and b with respect to the chosen failure criterion is also

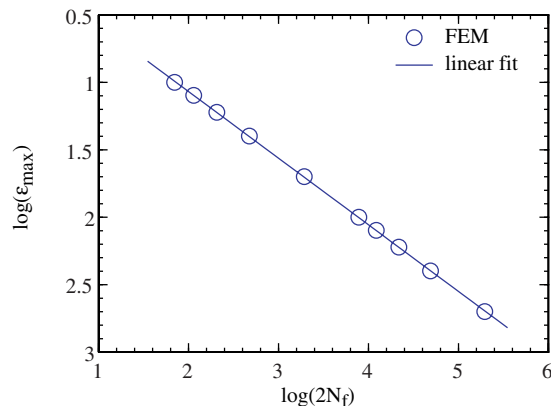


Fig. 12. The applied strain ϵ_{\max} versus the number of reversals to failure $2N_f$. Discrete points are numerical results, solid line is a linear fit with $\epsilon_{\max} = 0.83(2N_f)^{-0.49}$.

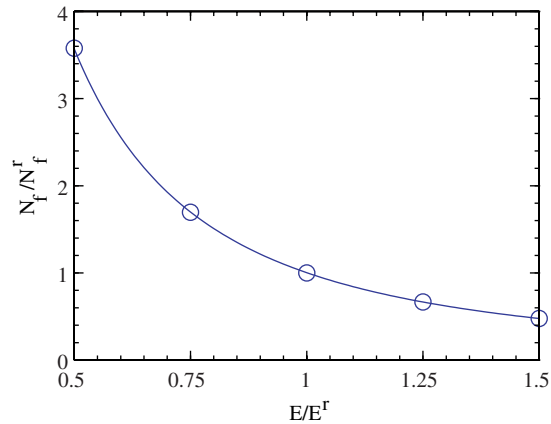


Fig. 13. Variation of the number of cycles to failure with the Young's moduli at constant maximum strain $\epsilon_{\max} = 1\%$. $N_f^r = 3899$ is the number of cycles to failure for the reference case with $E^r = 50$ and 16 GPa for the tin-rich and lead-rich phases, respectively. E is a multiple of these values. Discrete points are numerical results, solid line is a fit with: $N_f/N_f^r = (E/E^r)^{-1.83}$.

investigated. Using critical values of 25% and 75% resulted in the same value for the exponent b , namely, -0.49 . The coefficient a is found to depend on the failure criterion. Values of 1.0 and 0.69 are obtained using the 25% and the 75% criterion, respectively. The value obtained for the exponent b is within the range of experimentally obtained values for solder alloys (Kanchanomai et al., 2002; Lee et al., 2000).

The sensitivity of the parameters a and b in Eq. (25) to the elastic properties of the solder bump is also investigated. Two sets of calculations were performed using Young's moduli which are 50% lower and 50% higher than those listed in Section 2. The results of both sets were also well-fitted with a Coffin–Manson model. The values of the exponent b obtained for both sets are less than 1% different from 0.49 which is obtained previously for the data listed in Section 2. The coefficient a , however, is found to be dependent on the elastic moduli. Compared to the previous value of 0.83, values of 0.59 and 1.6 are obtained for the higher and lower Young's moduli, respectively. This leads to the conclusion that the higher the Young's moduli, the smaller the number of cycles to failure. Fig. 13 shows the number of cycles to failure as a function of the changes in the Young's moduli of the bump. It is clear from the fitting exponents in Figs. 12 and 13 that the dependence of the number of cycles to failure on the elastic moduli is as strong as their dependence on the applied strain.

For the range of applied strains 0.2–10%, the reaction force and the total effective damage show some scaling behavior. The reaction force normalized by the corresponding maximum force at the first cycle $F_x(N)/F_x^{\max}$ versus the normalized number of cycles N/N_f is identical for all values of applied strain. The same holds for the total effective damage D_{eff} when plotted against N/N_f . The shape of these plots looks like the shape like their respective ones in Figs. 10 and 11. This scaling holds only when $\sigma_f = 0$ in the damage evolution law of Eq. (6), which is the case here. In fact, this simply illustrates that damage accumulation is linear in this case. From the one-dimensional model discussed in Section 3.1 it is found that this scaling does not hold anymore for a nonzero value of the endurance limit as a result of a nonlinear damage accumulation.

4. Concluding remarks

Fatigue damage in a solder bump has been simulated in this paper using the finite element method. Damage is modeled using the cohesive zone method in which cohesive zones are embedded at physical

boundaries or interfaces which are potential locations for failure. The constitutive behavior of the cohesive zone is specified by a linear relation between the relative opening displacement at the cohesive zone and a corresponding traction. Material nonlinearity associated with dissipative mechanisms is accounted for by the inclusion of a damage variable into the cohesive zone constitutive law. The damage variable is supplemented with an evolution law to account for the gradual degradation of the solder material and the corresponding accumulation of damage throughout the cycling process. The evolution law is formulated such that it captures the main experimentally observed fatigue damage characteristics.

The cohesive zone approach seems promising in modeling fatigue damage in solder alloys. The numerical model prediction of the solder bump life-time was shown to have a good agreement with the Coffin–Manson model which has been one of the most common engineering models used for fatigue life-time predictions. The value obtained for the fatigue ductility exponent lies within the range of experimentally obtained values for solder alloys. It was demonstrated that this value does not depend on the variations in the elastic properties of the solder bump nor on the chosen failure criteria. The predicted life-time, however, was found to have a dependence on the elastic moduli of the bump as strong as its dependence on the applied strain.

The detailed simulation of each individual cycle is yet time consuming, especially for more realistic microstructure and large number of cycles. The time-reduction method explained in this study is only partly efficient since it still requires a detailed simulation of a large number of cycles. A major gain in the computational time can be achieved by the use of a time homogenization technique, which constitutes future work.

In conclusion, the original aspects of this work can be summarized as: (1) elaboration of a cohesive zone constitutive model for macroscopically quasi-brittle interfaces, using an *elasticity-based damage* formulation with a complex yet flexible description of the damage evolution; (2) elaboration of a constitutive model that enables the use of a relatively high initial stiffness, which avoids debatable assumptions that affect the overall compliance and which is a requirement for materials that fail in a quasi-brittle manner at the level of an interface; (3) application to a particular material of interest, solders in micro-electronics joints, for which it is known that failure concentrates at interfaces. This example illustrates that a ‘simple’ elasticity-based damage interfacial model already predicts the main trends observed (particularly in comparison with empirical fatigue models), in spite of the fact that the bulk material is not yet characterized nonlinearly, i.e., as a viscoplastic material.

Acknowledgment

This research is a part of the BTS-Senter project RIPOSTE (no. BTS99133), in cooperation with Philips Center for Industrial Technology and Philips Research Laboratory Eindhoven.

References

- Abdul-Baqi, A., 2002. Failure of Brittle Coatings on Ductile Metallic Substrates. PhD thesis, Shaker Publishing, The Netherlands.
- Basaran, C., Tang, H., Dishong, T., Searls, D., 2001. Computer simulations of solder joint reliability tests. *Advanced Packaging*.
- Chaboche, J., Feyela, F., Monerie, Y., 2001. Interface debonding models: a viscous regularization with a limited rate dependency. *International Journal of Solids and Structures* 38, 3127–3160.
- de Andres, A., Perez, J., Ortiz, M., 1999. Elastoplastic finite element analysis of three-dimensional fatigue crack growth in aluminum shafts subjected to axial loading. *International Journal of Solids and Structures* 36, 2231–2258.
- Ellyin, F., 1997. *Fatigue Damage, Crack Growth and Life Prediction*. Chapman Hall.
- Fatemi, A., Yang, L., 1998. Cumulative fatigue damage and life prediction theories: a survey of the state of the art for homogeneous materials. *International Journal of Fatigue* 20, 9–34.

- [Kanchanomai, C., Miyashita, Y., Mutoh, Y., 2002. Low cycle fatigue behavior and mechanisms of a eutectic Sn–Pb solder 63Sn/37Pb. *International Journal of Fatigue* 24, 671–683.](#)
- [Lee, W., Nguyen, L., Selvaduray, G., 2000. Solder joint fatigue models: review and applicability to chip scale packages. *Microelectronics Reliability* 40, 231–244.](#)
- [Lemaitre, J., 1996. *A Course on Damage Mechanics*. Springer-Verlag, Berlin.](#)
- [Martin, M., Vellinga, W., Geers, M., 2003. Quantitative microscopy of microstructural evolution in eutectic solders subjected to static thermal load. In: *Proceedings of the EuroSimE 2003 Conference*, Aix-en-Provence, France.](#)
- [Nguyen, O., Repetto, E., Ortiz, M., Radovitzky, R., 2001. A cohesive model of fatigue crack growth. *International Journal of Fracture* 110, 351–369.](#)
- [Roe, K., Siegmund, T., 2003. An irreversible cohesive zone model for interface fatigue crack growth simulation. *Engineering Fracture Mechanics* 70, 209–232.](#)
- [Tijssens, M., 2000. *On the cohesive surface methodology for fracture of brittle heterogeneous materials*. PhD thesis, Shaker Publishing, The Netherlands.](#)
- [Ubachs, R., Schreurs, P., Geers, M., 2003. Microstructure evolution of tin–lead solder. In: *Proceedings of the EuroSimE 2003 Conference*, Aix-en-Provence, France.](#)
- [Wu, P., van der Giessen, E., 1996. Computational aspects of localized deformations in amorphous glassy polymers. *European Journal of Mechanics, A/Solids* 15, 799–823.](#)
- [Xu, X.-P., Needleman, A., 1993. Void nucleation by inclusion debonding in a crystal matrix. *Modelling and Simulation in Materials Science and Engineering* 1, 111–132.](#)
- [Yang, B., Mall, S., Ravi-Chandar, K., 2000. A cohesive zone model for fatigue crack growth in quasibrittle materials. *International Journal of Solids and Structures* 38, 3927–3944.](#)
- [Zhang, X., Lee, S.-W., Pao, Y.-H., 2000. A damage evolution model for thermal fatigue analysis of solder joints. *Journal of Electronic Packaging* 122, 200–206.](#)